ORIGINAL ARTICLE

Iron-based and BRD$_4$-downregulated strategy for amplified ferroptosis based on pH-sensitive/NIR-II-boosted nano-matchbox

Lujing Geng[a], **Tong Lu**[b], **Huaqing Jing**[a], **Yue Zhou**[a], **Xiaoyang Liang**[a], **Jiao Li**[b,*], **Nan Li**[a,*]

[a]*Tianjin Key Laboratory of Drug Delivery & High-Efficiency, School of Pharmaceutical Science and Technology, Tianjin University, Tianjin 300072, China*
[b]*School of Precision Instruments and Optoelectronics Engineering, Tianjin University, Tianjin 300072, China*

Abstract   Ferroptosis (FPT), a novel form of programmed cell death, is characterized by overwhelming iron/reactive oxygen species (ROS)-dependent accumulation of lipid peroxidation (LPO). However, the insufficiency of endogenous iron and ROS level limited the FPT therapeutic efficacy to a large extent. To overcome this obstacle, the bromodomain-containing protein 4 (BRD$_4$)-inhibitor (+)-JQ1 (JQ1) and iron-supplement ferric ammonium citrate (FAC)-loaded gold nanorods (GNRs) are encapsulated into the zeolitic imidazolate framework-8 (ZIF-8) to form matchbox-like GNRs@JF/ZIF-8 for the amplified FPT therapy. The existence of matchbox (ZIF-8) is stable in physiologically neutral conditions but degradable in acidic environment, which could prevent the loaded agents from prematurely reacting. Moreover, GNRs as the drug-carriers induce the photothermal therapy (PTT) effect under the irradiation of near-infrared II (NIR-II) light owing to the absorption by localized surface plasmon resonance (LSPR), while the hyperthermia also boosts the JQ1 and FAC releasing in the tumor microenvironment (TME). On one hand, the FAC-induced Fenton/Fenton-like reactions in TME can simultaneously generate iron (Fe^{3+}/Fe^{2+}) and ROS to initiate the FPT treatment by LPO elevation. On the other hand, JQ1 as a small molecule inhibitor of BRD$_4$ protein can amplify FPT through downregulating the expression of glutathione peroxidase 4 (GPX4), thus inhibiting the ROS elimination and leading to the LPO accumulation. Both *in vitro* and *in vivo* studies reveal that this pH-sensitive nano-matchbox achieves obvious suppression of tumor growth with good biosafety and biocompatibility. As a result, our study points out a PTT combined iron-based/BRD$_4$-downregulated strategy for amplified ferrotherapy which also opens the door of future exploitation of ferrotherapy systems.

*Corresponding authors. Tel.: +86 22 13920235505, +86 22 13920437881.
E-mail addresses: jiaoli@tju.edu.cn (Jiao Li), linan19850115@163.com (Nan Li).

1. Introduction

Cell may die from regulated cell death (RCD) or accidental cell death (ACD) in the present study[1]. ACD is a kind of biologically uncontrolled process, while RCD is an active and essential process that not only maintains tissue homeostasis, but also causes inflammation-associated diseases[2]. The early RCD research started when the term "apoptosis" was illustrated in 1972 by John Kerr group[3]. A growing number of novel non-apoptotic forms of RCD have been identified including necroptosis, pyroptosis, ferroptosis, entotic cell death, netotic cell death, parthanatos, lysosome-dependent cell death, and autophagy-dependent cell death[2]. Tumor cells often have defects in executing cell death. To facilitate growth, tumor cells require higher levels of iron and lipid metabolism than normal cells, which also make tumor cells more susceptible to ferroptosis[4]. The ferroptosis (FPT) is a newly identified form of cell death, which is defined as the missed control of membrane lipid peroxidation (LPO) due to the inactivation of the glutathione peroxidase 4 (GPX4)[5−7]. As known that the high levels of iron and ROS are the characteristics of FPT[8,9]. Consequently, increasing the intracellular generation of ROS and concentration of iron are straightforward methods to induce the FPT. Recently, various chemicals have been widely designed for tumor therapy *via* Fenton/Fenton-like reactions in tumor microenvironment (TME), which could generate plentiful iron and ROS[10].

Fortunately, it has been reported that the ferric ammonium citrate (FAC) can be utilized as an iron-based reagent, which has the characteristic of good biocompatibility[11]. Moreover, FAC exhibits high reactivity towards the overexpressed hydrogen peroxide (H_2O_2) in TME to increase the content of iron (Fe^{2+}/Fe^{3+}) as well as hydroxyl radicals ($\cdot OH$) and perhydroxyl radicals ($HOO\cdot$)[12]. As shown in Eqs. (1)−(3), the series of ROS and iron (Fe^{2+}/Fe^{3+}) elevation is causative for membrane lipid peroxidation (LPO) which is identified as the executor of FPT[13−15] by encompassing the formation of lipid hydroperoxides (L-OOH) from polyunsaturated lipid (L-H) [Eq. (1)] and the construction of lipid peroxidation radicals (L-O·; L-OO·) from L-OOH [Eqs. (2) and (3)][16]. However, as shown in Eq. (4), those lipid hydroperoxides can be reduced into non-toxic hydroxy derivatives (L-OH) by GPX4 using glutathione (GSH) as a co-factor [Eq. (4)] to restrain the accumulation of LPO, which is defined as the process of ROS elimination[8,16,17]. Consequently, the FAC-induced ROS/ iron elevation is insufficient for the LPO accumulation due to the presence of ROS elimination, which subsequently causes the FPT treatment failure.

$$L\text{-}H + O_2 + \cdot OH + HOO\cdot + H^+ \rightarrow L\text{-}OOH \quad (1)$$

$$L\text{-}OOH + Fe^{2+} \rightarrow L\text{-}O\cdot + Fe^{3+} + H_2O \quad (2)$$

$$L\text{-}OOH + Fe^{3+} \rightarrow L\text{-}OO\cdot + Fe^{2+} + H_2O \quad (3)$$

$$L\text{-}OOH + GSH \rightarrow L\text{-}OH + GSSG \quad (4)$$
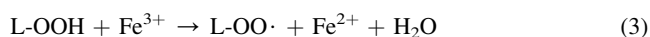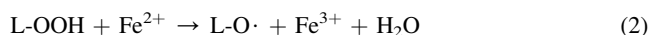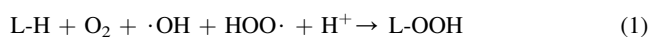
Moreover, as an iron-dependent, lipid peroxidation (LPO)-driven and glutathione peroxidase 4 (GPX4)-inhibitable form of cell death[18−20], FPT is confirmed to hold promise for tumor treatment and exhibits the advantage of bypassing the drug resistance of classical chemodrugs[13,21]. However, GPX4 is considered as ROS eliminator which can prevent the toxicity of ROS-induced intracellular lipid peroxides by its enzymatic activity[22] and remarkably limit the efficiency of FPT treatment. Notably, it has been reported that bromodomain-containing protein 4 (BRD_4), which is a member of bromodomain and extra terminal (BET) domain proteins family, can recognize acetylation sites and recruit transcription factors to regulate FPT-relative gene expression including *Gpx4* due to the four alpha helices structure[23−26]. As a result, BRD_4 as a super-enhancer of gene transcription[8,27] could inhibit the expression of GPX4 and ulteriorly facilitate the process of FPT by suppressing the ROS elimination. Interestingly, recent studies reveal that JQ1 can suppress the expression of FPT-associated gene (*Gpx4*) regulated by BRD_4 to block the endogenous ROS elimination, thus executing the LPO accumulation in tumor cells[28−31].

The aim of our study was to engineer the nano particles for photothermal-enhanced ferroptotic cell death in solid tumor. Herein, we develop JQ1/FAC-modified and zeolitic imidazolate framework-8 (ZIF-8)-coated gold nanorods to form the matchbox-like GNRs@JF/ZIF-8 nanoparticles for the amplified FPT treatment. In this study, mini-sized gold nanorods (GNRs) are employed as drug carries for their higher cellular uptake and satisfactory efficiency of near-infrared II (NIR-II) light absorption, which remarkably cause relatively deep site hyperthermia due to the localized surface plasmon resonance (LSPR) effect and thus promoting PTT effect and drugs (FAC and JQ1) releasing[32−34]. In addition, ZIF-8, which is stable in physiologically neutral conditions but degradable in acidic environment, could exhibit pH-sensitive property to prevent JQ1 and FAC from prematurely reacting[35,36]. The procedure of amplified FPT for suppressing proliferation and killing tumor cells can be explained as followed (Scheme 1): (1) After the matchbox shaped ZIF-8 degrading in lysosome acidic condition, NIR-II light-caused hyperthermia can promote PTT effect and boost the release of both JQ1 and FAC from the matches-like GNRs. (2) The FAC-induced ion/ROS production by Fenton/Fenton-like reaction directly yields plenty of ROS and iron (Fe^{2+}/Fe^{3+}), thereby facilitating the LPO production. (3) The released JQ1 downregulates BRD_4 protein and inhibits the process of ROS elimination based on decreased GPX4 enzymatic activity, which further accelerates the intracellular stacking of LPO. (4) The JQ1-caused inactivation of ROS elimination and the FAC-elevated ROS/iron jointly operated the LPO accumulation and FPT amplification. (5) In conclusion, the PTT combined FPT effect of GNRs@JF/ZIF-8 jointly realized the photothermal ferrotherapy, thus enhancing the antitumor efficacy to a large extent.

2. Materials and methods

2.1. Materials

Cetyltrimethyl ammonium bromide (CTAB, 99%) and mitochondrial membrane potential assay kit with JC-1 were both purchased from Beijing Solarbio Technology Co., Ltd. (China). (+)-JQ1 (98%) and ferric ammonium citrate (FAC) were obtained from Shanghai ALADDIN Reagent Co., Ltd. (China) and JIUDING Chemistry Co., Ltd. (Shanghai, China), respectively. Hydrogen tetrachloroaurate (III) (HAuCl$_4$, 99%), sodium borohydride (NaBH$_4$, 97%), methylene blue, 5,5'-dithiobis-(2-nitrobenzoic acid) (DTNB) and 2',7'-dichloro-fluorescein diacetate (DCFH-DA) were all bought from Tianjin Heowns Biochemical Technology Co., Ltd. (China). Methanol and ethanol (99.5%) were obtained from Tianjin Yuanli Chemical Co., Ltd. (China). Silver nitrate (AgNO$_3$, 99%) was gained from Tianjin Yingda Rare Chemical Reagents Factory (China). Hydroquinone (HQ, 99%) was obtained from Shanghai Rhawn Chemtech Co., Ltd. Zinc-phthalocyanine (ZnPc) was obtained from TCI (Shanghai, China) Development Co., Ltd. The reduced GSH Assay kit was purchased from Nanjing Jiancheng Bioengineering Institute. Zinc nitrate hexahydrate and H$_2$O$_2$ (30%) were obtained from Jiangtian Chemical Co., Ltd. (Tianjin, China). Liperfluo Kit was bought from Dojindo Molecular Technologies, Inc. (Rockville, Japan). All chemical reagents were of analytical grade and used as received without further purification.

2.2. Preparation of gold nanorods

The synthesis procedures of gold nanorods were carried out according to the seedless growth method[32,37,38]. Typically, 10 μL of HCl (1 mol/L) and 525 μL of aqueous hydroquinone (0.1 mol/L) were added to the solution containing 0.4 mL of HAuCl$_4$ (10 mmol/L), 10 mL of CTAB (0.1 mol/L) and 22.5 μL of AgNO$_3$ (100 mmol/L). The color of the mixture turned from orange to light brown after gentle mixing. After 15 min of stirring, 8 μL of freshly prepared ice-cold NaBH$_4$ solution (0.01 mol/L) was quickly added into the solution to move to the water bath kettle aging for 16 h at 35 °C under darkness. Finally, the GNRs solution was obtained by centrifuging at 15,000×g (H1750) for 20 min and rinsed twice with deionized water to get rid of excess CTAB surfactant.

2.3. Synthesis of nano-matchbox (GNRs@JF/ZIF-8)

MOFs structures have been demonstrated to be excellent hosts for metal nanoparticle (NPs). Metal NPs encapsulated in MOF structure hold great promise for a variety of applications. It has been reported that the metal nanoparticles can localize in the MOFs proes[39], shells[40] or between the layers[41]. The synthesis of metal crystals using MOFs as templates commonly yields metal crystals on the external surface of MOFs[42]. Thus, metal crystals are used as templates for the growth of MOFs to achieve the encapsulation of metal crystals in MOFs (metal@MOFs). In this study, ZIF-8 was fabricated using the GNRs as the templates to form the GNRs@JF/ZIF-8 structure (nano-matchbox) *via* the combined organic linkers and metal nodes.

The GNRs@JF/ZIF-8 nano-matchbox was synthesized through a three-step reaction as shown in Scheme 1. Firstly, for JQ1 loading, GNRs (4 mg) and JQ1 (2 mg/mL) were dispersed in methanol to stir

for 12 h under darkness at room temperature. The product of GNRs@JQ1 were then obtained by centrifugation (15,000×g, 6 min, H1750) and washed three times with ethanol. Secondly, the prepared GNRs@JQ1 was dissolved in 2 mL of ethanol, and then reacted with 3 mL of FAC saline solution through electrostatic interaction. After 12-h stirring, the GNRs@JQ1/FAC were purified by membrane dialysis (MWCO = 14 kDa) for 2 days with deionized water to remove the unloaded FAC. Then, the as-obtained product was dispersed in 1 mL of methanol for the next step. Ultimately, in order to prepare GNRs@JF/ZIF-8, we coated ZIF-8 onto the GNRs@JQ1/FAC to form the nano-matchbox structure. Briefly, 0.5 mL of the above solution containing GNRs@JQ1/FAC was added into Zn(NO$_3$)$_2$·6H$_2$O methanol solution (5 mL, 10 mmol/L) and stirred for 30 min at 60 °C. Then, we rapidly added 10 mL of 2-melthylimidazole methanol solution (10 mmol/L) into the above mixture and stirred for another 10 min. After that, the products were collected by centrifugation (15,000×g, 10 min, H1750) and washed three times with ethanol to disperse in 5 mL of deionized water and stored at 4 °C for further experimental usages.

2.4. Drug loading and pH-responsive drug release experiment

The loading capacity and efficacy of JQ1 in GNRs@JF/ZIF-8 were measured by UV–Vis maximum absorbance at 280 nm, while that of FAC was measured by ICP–OES through detecting the Fe content. Moreover, the pH-responsive drug releasing profiles of JQ1 and FAC were assessed in pH 7.4 and 5.0 solutions, which mimicked physiological and lysosome media, respectively. Meanwhile, laser (1064 nm, 1.0 W/cm^2, 5 min) irradiated on the solutions on 4 and 8 h, respectively. TEM analysis was applied to evaluate the pH-sensitive capability of ZIF-8 shell in different conditions directly.

2.5. In vitro photothermal performance of GNRs@JF/ZIF-8

Various concentrations of GNRs@JF/ZIF-8 (6.25, 12.5, 25, 50 and 100 mg/mL) aqueous dispersions were placed in the 1.5-mL centrifuge tubes and irradiated under the 1064 nm laser (1.0 W/cm^2) for 5 min. Meanwhile, an infrared thermal imager was used to monitor and capture the photothermal images of different dispersion every 20 s. Besides, as in the reported measuring methods, the photothermal conversion efficacy (η) of GNRs@JF/ZIF-8 with 1064 nm laser irradiation was obtained by calculating the formula [Eq. (5)][43]:

$$\eta\,(\%) = \frac{hS(T_{max} - T_{surr}) - Q_s}{I\left(1 - 10^{-A_{1064}}\right)} \times 100 \qquad (5)$$

where h (W·cm^{-2}/K) stands for the heat transfer coefficient, S (cm^2) represents the surface area of the container, T_{max} (K) is the maximum steady temperature while T_{surr} (K) is the ambient temperature of the surroundings, Q_s (mW) refers to the heat loss from light absorbed by the container, I (1.0 W/cm^2) indicates incident laser power, A_{1064} means the absorbance of samples at 1064 nm.

2.6. Reactions between GNRs@JF/ZIF-8 and GSH

Different concentrations of GSH (0.5, 1.0, 2.0, 5.0 and 10 mmol/L) and GNRs@JF/ZIF-8 (200 μg/mL) were mixed at room temperature and allowed to set for 20 min. Then, the supernatant was collected after centrifugation and added to a mixture of MB

(30 μL, 1 mg/mL)/H_2O_2 (30 μL, 1 mol/L) solution to a total volume of 3 mL. After 30 min of reaction at 37 °C, the final supernatant was examined by UV−Vis maximum absorbance at 664 nm. Similarly, UV−Vis spectra were also obtained according to the method described above with different pH conditions.

2.7.   In vitro ·OH generation and GSH detection

The generation of ·OH was then detected. In brief, solutions of 200 μg/mL GNRs@JF/ZIF-8, 1 mmol/L GSH, 10 mmol/L H_2O_2 and 10 mmol/L 5,5-dimethyl-1-pyrroline N-oxide (DMPO) were prepared to respectively mix with 4 different groups: (I) H_2O_2 only, (II) H_2O_2 + GNRs@JF/ZIF-8, (III) H_2O_2 + GSH + GNRs@JF/ZIF-8, (IV) H_2O_2 + GSH + GNRs@JF/ZIF-8 +NIR-II. Finally, the generation of ·OH in above groups was measured by the ESR spectroscopy.

To explore the GSH consumption capability of the GNRs@JF/ZIF-8, 5,5′-dithiobis-(2-nitrobenzoic acid) (DTNB) solution (2 mg/mL, 30 μL), GSH solution (10 mmol/L, 30 μL) and various volume of GNRs@JF/ZIF-8 (200 μg/mL, 225, 450, 900 and 1800 μL) were mixed at room temperature and added deionized water to a total volume of 3 mL to obtain GNRs@JF/ZIF-8 solutions with different concentration gradients. After 20 min of reaction, the supernatant was collected to determine the absorbance subsequently.

2.8.   GNRs@JF/ZIF-8 induced LPO under GSH and Fe^{2+} in vitro

Briefly, as the reported method instructs[5], lipids (cell membrane extracted from 4T1 cells) were divided into 6 groups, which were mixed with: (I) H_2O_2, (II) nanoparticle (GNRs@JF/ZIF-8), (III) GSH, (IV) Fe^{2+} ($FeSO_4$), (V) H_2O_2 + nanoparticle + Fe^{2+}, (VI) H_2O_2 + nanoparticle + GSH, respectively. After incubating overnight at room temperature, the color change of the samples was observed.

2.9.   Cellular uptake studies

For the exploration of the GNRs@JF/ZIF-8 cellular uptake profile, the 4T1 cells were firstly seeded in the CLSM dishes. When the cell density reached about 10^6/well, the culture medium was discarded and replaced with GNRs@JF/ZIF-8 labeled FITC. After 1, 6, 10 and 12 h of culturing, Lysotracker Red and DAPI were sequentially added to stain endosomes and nuclei for 1 h and 10 min, respectively. After the staining, the cells were washed with PBS three times to observe and image by the confocal laser scanning microscopy (CLSM).

2.10.   In vitro cytotoxicity detection

To evaluate the cellular toxicity, CCK-8 assay and co-stained test were jointly employed to assess the cytotoxicity of different formulations. Firstly, 4T1 cells were pre-seeded into a 96-well cell culture plate and incubated in 5% CO_2 at 37 °C under dark condition for 24 h. Then, various concentrations of GNRs@JF/ZIF-8 (0, 20, 40, 60, 80, 100 μg/mL) were respectively added into each well and co-incubated for 6 h. For phototoxicity groups, each well of cells was continually irradiated with 1064 nm laser (1.0 W/cm², 5 min) and cultured for another 18 h. Subsequently, CCK-8 solution (0.1 mol/L, 10 μL) was added into each well at 37 °C, followed by discarding the culture medium after 4 h. The

absorbance at 450 nm of each well was detected by utilizing a microplate reader to measure the relative cellular viability eventually.

Except for CCK-8 kit assay, AM/PI co-stained experiment was also applied to assess the cytotoxicity of the nanoparticles. Initially, 4T1 cells were seeded in 6-well plates. After 24 h culturing, the culture medium was removed and respectively replaced with (I) PBS, (II) PBS + NIR (1064 nm, 1.0 W/cm², 5 min), (III) GNRs@JQ1/ZIF-8, (IV) GNRs@FAC/ZIF-8, (V) GNRs + NIR-II (1064 nm, 1.0 W/cm², 5 min), (VI) GNRs@JF/ZIF-8 and (VII) GNRs@JF/ZIF-8 + NIR-II (1064 nm, 1.0 W/cm², 5 min). Afterwards, the cells were stained with Calcein-AM (4 μmol/L, 488/515 nm) and PI (4 μmol/L, 535/617 nm) for 15 min and imaged by CLSM.

2.11.   Western blot analysis

Western blot was applied to measure the level of FPT-related protein expression. Briefly, 4T1 cells were cultured in 6-well plates and treated with various formulations, then all cells were harvested and placed in 1.5-mL centrifuge tubes, followed by adding 200 μL of RIPA lysis buffer containing PMSF (Beyotime, China). After 30 min lysis in ice box, the total proteins were extracted through high speed refrigerated table centrifuge (GTR16-2) (12.000 rpm, 4 °C, and 10 min). Bicinchoninic acid (BCA) assay was then used for protein determination. Afterwards, specific antibodies were used for Western blot assay, in which anti-BRD_4 (BM4286, 1:1000) and anti-GPX4 (BM5231, 1:10,000, and anti-β-actin (BM0627, 1:5000) were acted as the internal controls. After the primary antibodies' treatments, the membranes were further incubated with goat anti-rabbit IgG H&L (ZM0591, 1; 5000) for 1.5 h at room temperature. Finally, immunoreactions were analyzed through a Champchemi 610 plus imager.

2.12.   Intracellular GSH measurement

To determine the depletion of GSH in cells after treated with different formulations, 4T1 cells were seeded in 6-well plates and cultured for 24 h at 37 °C. The media were then removed and respectively replaced with (I) PBS, (II) GNRs@JF/ZIF-8 (50 μg/mL), and (III) GNRs@JF/ZIF-8 (100 μg/mL). After 6 h incubating, all groups were exposed to 1064 nm laser irradiation (1.0 W/cm², 5 min). Cells were then collected after PBS washing and centrifugation (1200 rpm, 3 min, H1750), followed by ultrasonication for 10 min on ice. Afterwards, the cell lysate was detected following the commercial GSH Assay kit protocol.

2.13.   In vitro cytoplasmic ROS level detection

To detect the Fenton-induced ·OH generation, the generated ROS of the cells was evaluated by ROS sensitive probe named DCFH-DA. Briefly, the 4T1 cells were typically seeded in the CLSM dishes with a density of 10^5/mL. Cells were then respectively co-incubated with (I) PBS (control), (II) PBS + NIR (1064 nm, 1.0 W/cm², 5 min), (III) GNRs@JQ1/ZIF-8, (IV) GNRs@FAC/ZIF-8, (V) GNRs + NIR-II (1064 nm, 1.0 W/cm², 5 min), (VI) GNRs@JF/ZIF-8 and (VII) GNRs@JF/ZIF-8 + NIR-II (1064 nm, 1.0 W/cm², 5 min). The media were removed after 12 h, followed by adding DCFH-DA (10 μm/L) into each well to incubate at 37 °C for 20 min. Then, cells were collected after washing with PBS thrice, thereafter, they were incubated with DAPI (10 μg/mL, 1 mL, 10 min) for the next observation by CLSM.

2.14. Measurement of mitochondrial membrane potential and LPO generation

JC-1 probe was usually applied to stain cells to measure the mitochondrial membrane potential. In a typical method, 4T1 cells were seeded in CLSM dishes for 24 h and respectively incubated with (I) PBS (control), (II) PBS + NIR (1064 nm, 1.0 W/cm^2, 5 min), (III) GNRs@JQ1/ZIF-8, (IV) GNRs@FAC/ZIF-8, (V) GNRs + NIR-II (1064 nm, 1.0 W/cm^2, 5 min), (VI) GNRs@JF/ZIF-8 and (VII) GNRs@JF/ZIF-8 + NIR-II (1064 nm, 1.0 W/cm^2, 5 min). After 12 h culturing, cells were incubated with DMEM containing JC-1 (1 µg/mL) at 37 °C for 30 min. The Leica SP 8 microscopy was then applied to record images of cells.

Similarly, in order to explore the mechanism of FPT, the Liperfluo, another selective fluorescence probe which can be oxidized by LPO, was used to investigate the intracellular LPO level. The concentration of Liperfluo was fixed at 10 µmol/L (Ex = 532 nm, Em = 535−650 nm).

2.15. Hemolysis assay

The hemolytic effect of nanoparticles was evaluated by the following procedures. In detail, the blood samples (1 mL) were obtained from the mice and diluted with PBS (2 mL). Then the red blood cells (RBCs) were separated from serum after centrifuging (2000 rpm, 10 min) and washed 4 times. Subsequently, 10 mL of PBS was added to prepare RBCs suspension. Then 200 µL of RBCs suspension was treated with 1 mL of GNRs@JF/ZIF-8 solution (40, 50, 60, 80, 100 µg/mL), deionized water (positive control) and PBS (negative control), respectively, to incubate at 37 °C for 2 h. All supernatants were collected after centrifugation (1200 rpm, 10 min, H1750) and added to a 96-well plate to record the absorbance at 570 nm via the microplate reader. Eventually, the hemolysis percentage of RBCs was calculated according to Eq. (6) shown below:

$$\text{Hemolysis } (\%) = \frac{A_{\text{sample}} - A_-}{A_+ - A_-} \times 100 \qquad (6)$$

where A_{sample} stand for the absorbance of samples at 570 nm, while A_+ and A_- represent the absorbance of positive and negative control at 570 nm, respectively.

2.16. Mitochondria morphology observation

To intuitively observe the FPT-induced changes of cellular morphologies before and after treatment, 4T1 cells were seeded in 10-cm dishes treated with formulation GNRs@JF/ZIF-8+NIR (1064 nm, 1.0 W/cm^2, 5 min) and PBS + NIR (1064 nm, 1.0 W/cm^2, 5 min) for comparison, respectively. After 12 h culturing, cells were harvested and suspended in 2 mL of glutaraldehyde solution (electron microscopy-grade) and stored at 4 °C for further TEM imaging analysis.

2.17. Animal models and antitumor in vivo treatment

Female BALB/c mice (4−6 weeks old) were ordered from Huafukang Biological Technology Co., Ltd.(Beijing, China). The whole experimental procedures were carried out at the Laboratory Animal Center of the Chinese Academy of Medical Sciences Institute of Radiology in Tianjin and in compliance with the institution's guidelines for maintenance and use of laboratory animals. All the animals in this study received humanistic care in accordance with humanitarian and guidelines of Tianjin University.

Firstly, 4T1 cells were injected subcutaneously into the right axilla of each BALB/c mouse to establish the tumor model. When the volume of tumor entity reached ∼100 mm^3, 4T1 tumor-bearing mice were randomly divided into 7 groups (n = 5 per group) and intravenously injected with: PBS (with or without NIR), GNRs@JQ1/ZIF-8, GNRs@FAC/ZIF-8, GNRs (with NIR), GNRs@JF/ZIF-8 (with or without NIR) (100 µL, 1 mg/mL) on Days 0, 3, and 6. For the illumination groups, mice were successively administrated with 1064 nm laser (1.0 W/cm^2) 12 h after the injection to monitor IR images utilizing the preceding infrared camera. During the entire therapeutic period, the tumor size and weight of mice were recorded every other day. Tumor volume was simply measured with a vernier caliper and calculated according to Eq. (7) shown below:

$$\text{Tumor volume} = (\text{Tumor length}) \times (\text{Tumor width})^2/2 \qquad (7)$$

Additionally, tumors and major organs (heart, liver, spleen, lung and kidney) were isolated from sacrificed mice at the end of the experimental process for further study via biodistribution, hematoxylin and eosin (H&E), immunofluorescence and immunohistochemical (BRD$_4$ and GPX4) staining (Supporting Information).

2.18. In vivo MSOT/CT imaging dual-mode imaging

For multi-spectral optoacoustic tomography (MSOT) imaging, GNRs@JF/ZIF-8 (100 µL, 2 mg/mL) was injected into the tail vein of tumor-bearing mice. Images were recorded for MSOT analysis at interval time points (1, 6, 12, and 24 h). Then the signal intensities for MSOT were accordingly determined via the high-resolution photoacoustic tomography system (15 MHz for the center frequency of the transducer).

For computed tomography (CT) imaging, 100 µL of GNRs@JF/ZIF-8 solution (4 mg/mL) and iohexol (contrast agent as control) were injected into the mice whose tumor reached a diameter around 100 mm^3. Then mice were scanned through the micro CT scanner (Quantum FX; PerkinElmer, United States) for imaging at the time points coinciding with the MSOT imaging.

2.19. In vivo biodistribution

Briefly, after treatment with GNRs@JF/ZIF-8 (100 µL, 2 mg/mL), major organs (heart, liver, spleen, lung, and kidney) and tumor sections from tumor-bearing mice were obtained at 1, 12, 24 h post-injection (n = 3 each group) and weighted prior to digesting in 5 mL of nitrohydrochloric acid (metal-oxide-semiconductor grade). Then, 1 mL of 30% H$_2$O$_2$ was added into the dissolved solutions to be transferred to the heating digestion tanks to volatilize the acid. After that, the residual liquid was diluted to 10 mL by deionized water. Eventually, the Au, Fe, Zn contents of samples were finally quantified by ICP−MS.

3. Results and discussion

3.1. Synthesis and characterization of nano-matchbox (GNRs@JF/ZIF-8)

The whole procedure of GNRs@JF/ZIF-8 preparation has been integrally shown in Scheme 1A. Briefly, the gold nanorods (GNRs) were fabricated on the basis of seedless method, which was more time-saving and steady than the seed method[44,45].

Simply summarized, we reduced the chloroauric acid (HAuCl$_4$) by the weak reducing hydroquinone (HQ) in the presence of small dose of silver nitrate and cetyltrimethylammonium bromide (CTAB). JQ1 and FAC were then loaded onto the surface of GNRs through the electrostatic attraction. After that, we deposited GNRs@JQ1/FAC (nano-match) with ZIF-8 to form the GNRs@JF/ZIF-8 (nano-matchbox) *via* the combined organic linkers and metal nodes[42].

The formation process of GNRs@JF/ZIF-8 was exhibited in transmission electron microscopy (TEM) images. We obtained the matches-like GNRs with average diameter of 50 nm × 6 nm (length × width) with an aspect ratio of ∼8.3 (Fig. 1A). Similar to the empty matchbox-like ZIF-8 (Fig. 1B), the average diameter of final formulation GNRs@JF/ZIF-8 was around 220 nm (Fig. 1C), which was consistent with the results of dynamic light scattering (DLS) analysis (Supporting Information Figs. S1A and S1B). From the images, the nano-matchbox structure of enclosed GNRs within ZIF-8 was clearly observed, illustrating the successful synthesis of the GNRs@JF/ZIF-8. Besides, the corresponding selected area electron diffraction (SAED) showed the superimposed diffraction rings at (111), (200), (220), (311), (331) and (420), which proved the polycrystalline structures of GNRs (Fig. 1D). Furthermore, the peaks of X-ray diffraction at 38.184°, 44.392°, 64.576°, 77.547°, 110.798° and 115.259° were consistent with the (111), (200), (220), (311), (331) and (420) crystal planes of Au (JCPDS 04-0784), respectively (Fig. 1E). Besides, from the X-ray photoelectron spectroscopy (XPS) spectrum, the Au 4f$_{5/2}$ and Au 4f$_{7/2}$ spectra were located at around 87.7 and 84.0 eV, ulteriorly revealing that Au existed as the zero-valent state (Fig. 1F). What's more, the UV−Vis absorption spectra of various formulations were partly located in NIR-II window. Specifically, the GNRs@JF/ZIF-8 exhibited extended NIR absorption up to 1100 nm, which portended the good photothermal efficiency under NIR-II irradiation (Fig. 1G). In addition, the zeta potential of various formulations (GNRs, JQ1, GNRs@JQ1/FAC and GNRs@JF/ZIF-8) were 42.2, −20.8, 12.3 and 21.7 eV, respectively, which provided evidence that JQ1 and FAC were successfully co-loaded onto the GNRs through opposite charge attraction (Supporting Information Fig. S2). Besides, FT-IR spectra of JQ1, FAC and GNRs@JQ1/FAC from 400 to 4000 cm^{-1} were shown in Supporting Information Fig. S3, in which the absorption peaks at 3000 cm^{-1} and 3500 cm^{-1} of GNRs@JQ1/FAC confirmed the loading of JQ1 and FAC, respectively. The energy-dispersive X-ray spectroscopy (EDS) spectrum of Cl, Fe, Zn, and Au elements in GNRs@JF/ZIF8 was detected by a high-resolution TEM (Thermo Fischer Talos F200x, Czech Republic) in Supporting Information Fig. S4 and Table S1. The stability of GNRs@JF/ZIF-8 was then evaluated by particle size variation. There was no distinct change in hydrodynamic diameters during 7-day incubation with water, PBS, Dulbecco's modified Eagle's medium (DMEM) and Fetal bovine serum (FBS), respectively, illustrating the fair stability of GNRs@JF/ZIF-8 under different physiological condition (Supporting Information Fig. S5).

3.2. pH-sensitive capability of ZIF-8

To explore the pH-sensitive capability of the ZIF-8, we subsequently mimicked various conditions with different pH solutions. As illustrated in Supporting Information Fig. S6, ZIF-8 still presented regular cubic morphology after incubation with pH 7.4 buffer at 24 h, demonstrating its low sensibility under

physiological condition. When incubated with pH 6.5 buffer for 24 h, however, the core of ZIF-8 was etched gradually and exhibited irregular appearance. What's more, it showed obvious brokenness in pH 6.0 buffer and even enhanced pH-sensibility in pH 5.0 buffer.

3.3. In vitro photothermal effect of the GNRs@JF/ZIF-8

The GNRs could convert the irradiation to heat owing to the NIR-II absorption by localized surface plasmon resonance LSPR[43]. To measure the photothermal effect, various concentration groups (0.0625, 0.125, 0.25, 0.5 and 1 mg/mL) of GNRs@JF/ZIF-8 were detected upon the 1064 nm laser (1.0 W/cm^2, 7 min) (Fig. 1H). The temperature rose slightly from 25 °C to 31 °C at a low concentration of 0.0625 mg/mL, while it increased distinctly as the concentration increased from 0.125 mg/mL to 1 mg/mL. Typically, the temperature of the GNRs@JF/ZIF-8 increased from 32 °C to 55 °C within 7 min at a concentration of 1 mg/mL, indicating the good NIR-induced photothermal effect. Besides, the corresponding photothermal conversion efficiency was calculated to be 23.76% according to the fitting cooling curve *in vitro* by exposing GNRs@JF/ZIF-8 solution (500 μg/mL) to the continuous 1064 nm laser (1.0 W/cm^2) for 480 s (Fig. 1I).

3.4. pH-responsive drug releasing efficiency of GNRs@JF/ZIF-8

In this study, the loading ratios were correspondingly calculated to be 6.5% (*w/w*, Fe) and 16.3% (*w/w*, JQ1), which were respectively detected by ICP−OES and UV−Vis spectroscopy (Supporting Information Figs. S7A and S7B). The JQ1 and FAC released from GNRs@JF/ZIF-8 were assessed in pH 7.4 and 5.0 buffer, which respectively mimicked physiological and lysosome conditions. Specifically, the release rates of JQ1 and FAC were measured to be 33.8% and 41.3% at pH 5.0 at 24 h, respectively, which were higher than those at pH 7.4 due to the degradation of ZIF-8 in lower pH solution. Additionally, the laser-induced hyperthermia significantly accelerated the releasing (Supporting Information Fig. S8), indicating that the release capability of GNRs@JF/ZIF-8 could be enhanced by NIR irradiation.

3.5. In vitro Fenton-induced ROS generation

As illustrated in Fig. 2A, by Fenton-like reaction, the GSH-reduced Fe^{2+} could react with H$_2$O$_2$ to produce ·OH, thus causing the MB degradation. Additionally, the GSH depletion was measured by Ellman's assay with 5,5-dithio-bis-(2-nitrobenzoic acid) (DNTB) probe. As expected, the relative GSH level exhibited distinct decrease with the increased GNRs@JF/ZIF-8 concentrations (30−240 μg/mL) (Fig. 2B). The obvious color change (inset of Fig. 2B) further illustrated the consumption of GSH by the GNRs@JF/ZIF-8 nano-matchbox. What's more, the degradation rate of MB was increased with the raised concentrations (0−3 mmol/L) of GSH, demonstrating the enhancement of ·OH generation (Fig. 2C). Inspired by the degradable properties of the ZIF-8 under acidic conditions, we investigated the effect of pH value on ·OH generation. From the UV−Vis absorption spectroscopy and the color change (inset images), it was obvious that the degradation rate of MB gradually increased with the decreased pH value (7.4−5.0) due to FAC releasing from the pH-sensitive ZIF-8 as well as the PTT and H$^+$ facilitated the Fenton reactions to some extent (Fig. 2D).
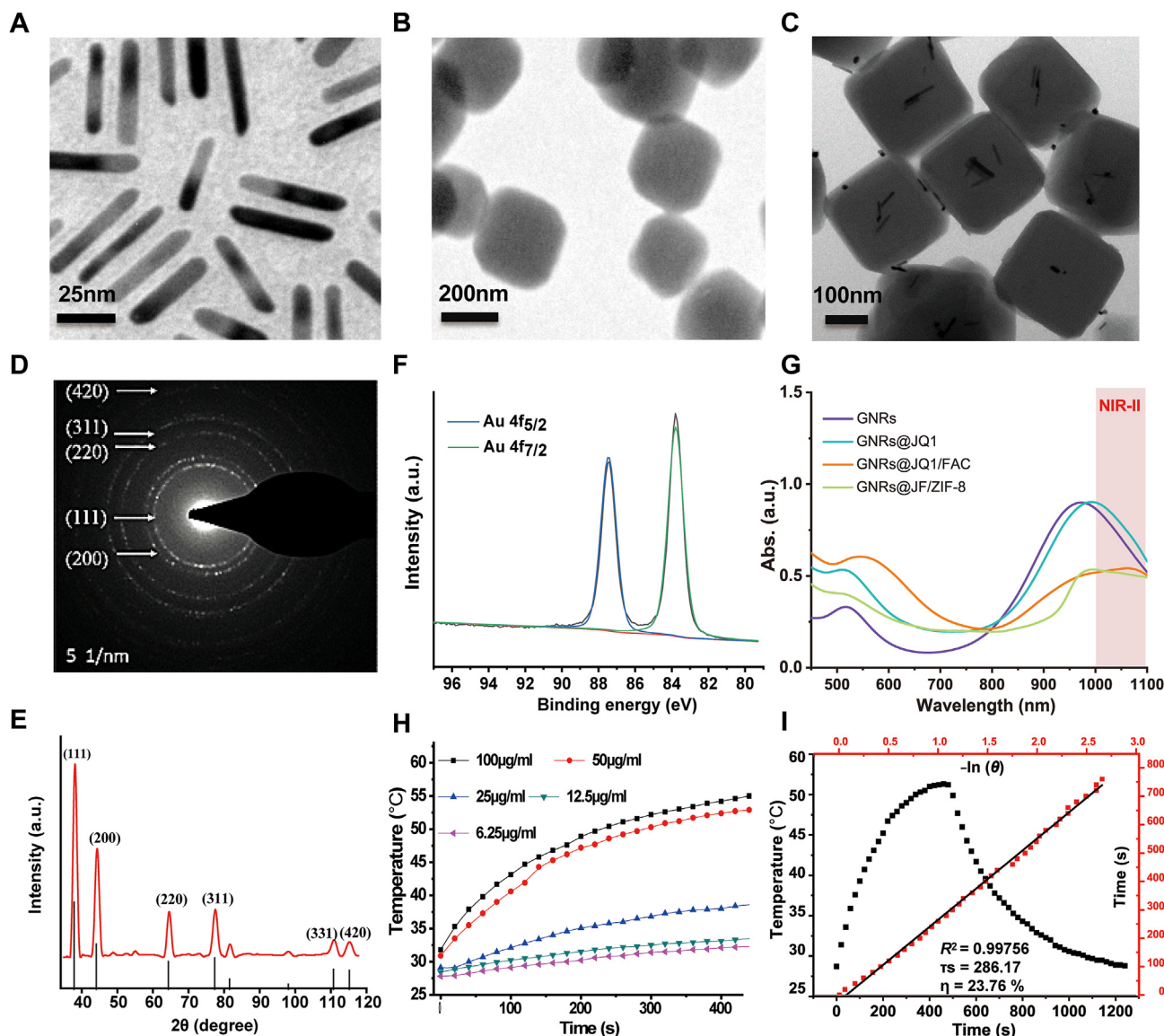
Figure 1 (A−C) TEM images of GNRs, ZIF-8 and GNRs@JF/ZIF-8. (D) SAED pattern of the GNRs. (E) XRD spectrum of GNRs. (F) Au 4f XPS spectrum. (G) UV−Vis spectra of GNRs, GNRs@JQ1, GNRs@JQ1/FAC, GNRs@JQ1/FAC/ZIF-8 (GNRs@JF/ZIF-8). (H) Photothermal performance of GNRs@JF/ZIF-8 with different concentration exposed to 1064 nm laser (1 W/cm², 7 min). (I) Photothermal effect of GNRs (500 μg/mL) under 1.0 W/cm², 1064 nm irradiation for 480 s and the corresponding linear relationship between −ln (θ) and time points.

We subsequently assessed the degradation rate of MB under various conditions. For the MB + GNRs@JF/ZIF-8 + H_2O_2 group, about 52.5% MB was degraded in 40 min, compared with 74.5% degradation rate in the MB + GNRs@JF/ZIF-8 + H_2O_2 + GSH group. Besides, the content of MB decreased sharply by 85.4% under the 1064 nm laser irradiation (Fig. 2E), demonstrating that the NIR-II laser boosted the drug releasing to a large extent. Specifically, the degradation rate was abided by the pseudo-first order reaction kinetics: $-\ln (C/C_0) = k_{app}\, t$, wherein, C_0 and C represented the initial MB concentration and concentration at time t (min), respectively, and k (min⁻¹) indicated the reaction rate constant. The respond of $-\ln (C/C_0)$ to the reaction times on the basis of above equation was well illustrated in Fig. 2F. In detail, the apparent rate constants were calculated to be

0.0014, 0.0217, 0.0402 and 0.0601 min⁻¹ for H_2O_2, GNRs@JF/ZIF-8 + H_2O_2, GNRs@JF/ZIF-8 + GSH + H_2O_2 and GNRs@JF/ZIF-8 + GSH + H_2O_2 + NIR, respectively (Supporting Information Table S2).

Eventually, to identify the level of ·OH generation, the ESR spectra were measured under different conditions (Fig. 2G). The obtained data exhibited the strongest ESR intensity in the group of H_2O_2 + GSH + GNRs@JF/ZIF-8 + NIR, which verified that the ·OH generation was boosted by NIR-II laser irradiation. According to above results, we concluded that the Fe (III) in GNRs@JF/ZIF-8 could be initially reduced to Fe (II) by the GSH, followed by reacting with H_2O_2 to generate ·OH under the irradiation of NIR-II laser, thus resulting in the MB degradation.
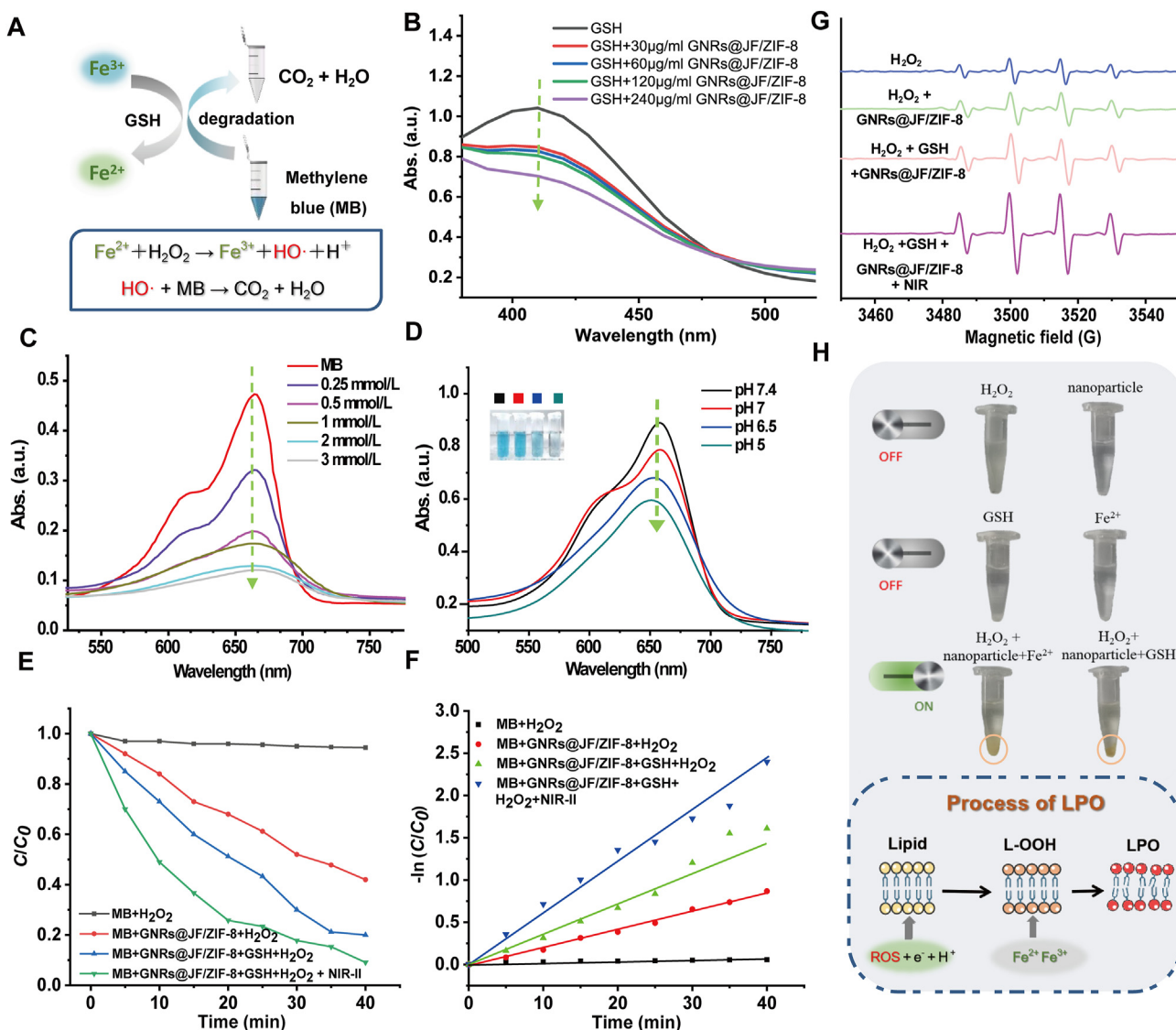
Figure 2 (A) Schematic illustration of MB degradation by GNRs@JF/ZIF-8. (B) GSH consumption (100 μmol/L) under the reduction with various concentrations of GNRs@JF/ZIF-8. (C) Degradation of MB by ·OH treated with H_2O_2 (10 mmol/L) and different concentrations of GSH. (D) MB degradation under different pH PBS. (E) MB degradation efficiency in different conditions. (F) Corresponding responses of $\ln(C/C_0)$ to the reaction time based on (E). (G) ESR spectra of ·OH spin adduct generated by different groups. (H) The process of transition from Lipid to LPO.

3.6. In vitro LPO measurement

Additionally, we investigated the role of iron in the process of lipid peroxidation (LPO) accumulation (Fig. 2H). The mechanism of LPO generation was explained by the schematic diagram in the bottom of Fig. 2H. The lipids (L-H) could be converted to the LPO in the presence of Fe^{3+} and Fe^{2+} *via* Fenton/Fenton-like reactions. In this study, 12 mg of lipids were separated into 6 groups equally. Lipids were then incubated with H_2O_2, nanoparticle (GNRs@JF/ZIF8), GSH and Fe^{2+}, respectively. Specifically, the green lock stood for the LPO generation. From the results, there was no obvious change of lipids after treating with individual H_2O_2, Fe^{2+}, GSH or nanoparticle, which meant that they could not give rise to LPO generation, while significant yellow precipitation appeared in GNRs@JF/ZIF-8-administrated groups in the presence of Fe^{2+} or GSH, indicating that the iron (Fe^{3+}/Fe^{2+}) could trigger LPO

generation by Fenton/Fenton-like reactions with H_2O_2 (Supporting Information Fig. S9).

3.7. In vitro cell viability and cellular uptake studies

The cytotoxicity of various formulations to 4T1 cells were carried out by CCK-8 assay. As demonstrated in Fig. 3A, PBS (with or without NIR) groups verified the non-cytotoxicity of 4T1 cells, while mild cytotoxicity was observed in the GNRs@JQ1/ZIF-8 and GNRs@FAC/ZIF-8-treated groups due to the insufficient LPO accumulation, GNRs (with NIR)-treated group exhibited stronger cytotoxicity due to the photothermal effect. However, the cell viability of GNRs@JF/ZIF-8-treated group declined remarkably, suggesting that the production of ROS/iron by Fenton/Fenton-like reaction amplified the effect of FPT. Besides, after 1064 nm laser irradiation on the GNRs@JF/ZIF-8 group, the
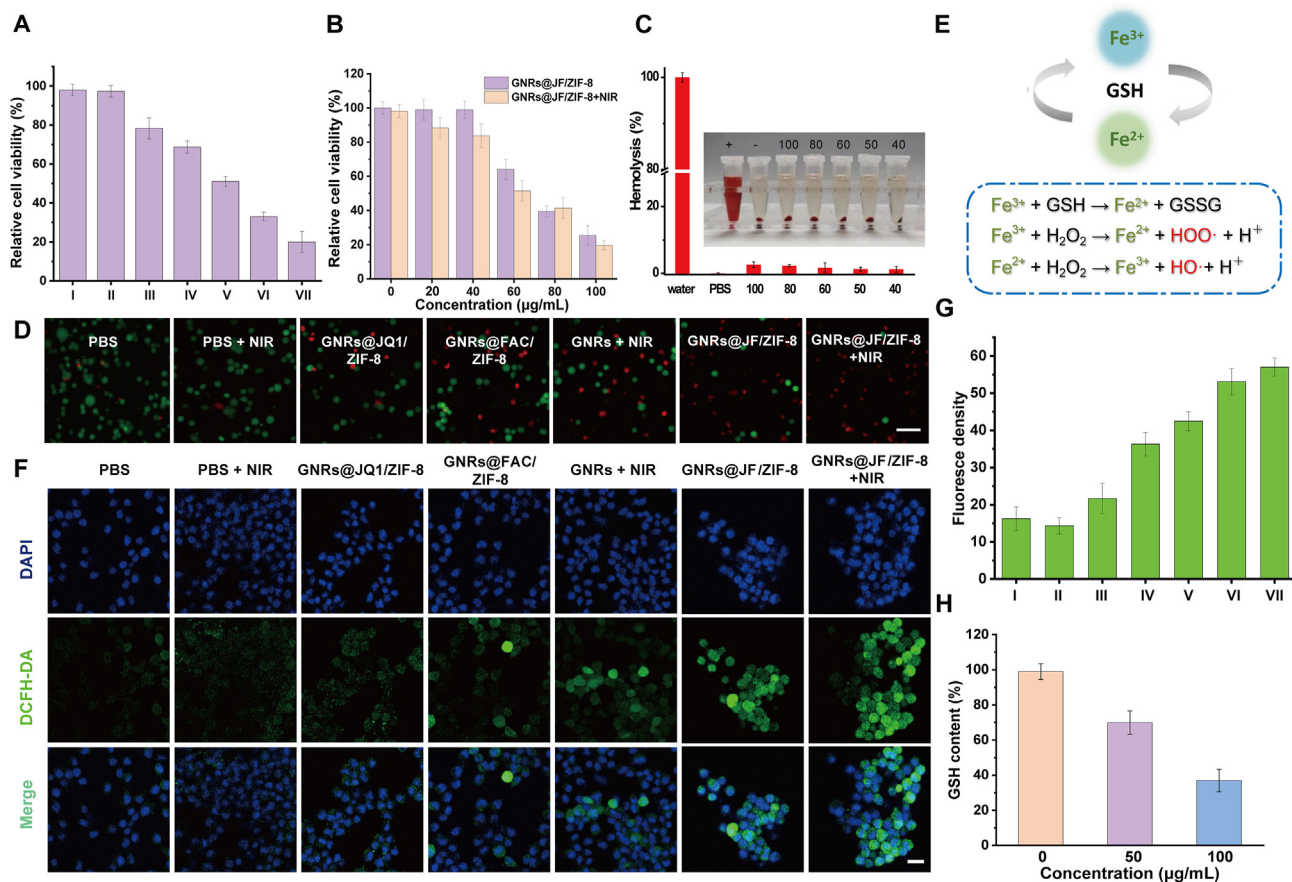
Figure 3 (A) Cell viabilities after treated with various conditions: (I) PBS group, (II) PBS + NIR, (III) GNRs@JQ1/ZIF-8, (IV) GNRs@FAC/ZIF-8, (V) GNRs + NIR, (VI) GNRs@JF/ZIF-8 and (VII) GNRs@JF/ZIF-8 +NIR, respectively. (B) Cell viabilities after treated with various concentrations of GNRs@JF/ZIF-8 by CCK-8 assay of 4T1 cells. (C) The GNRs@JF/ZIF-8 after incubation with RBCs at various concentrations for 2 h, utilizing PBS and deionized water as negative ($-$) and positive ($+$) control, respectively. Inset: hemolysis images after centrifugation. (D) The live/dead cell images of 4T1 cells stained by AM/PI after incubation with various groups (scale bar $=$ 100 μm for all panels). (E) FAC-induced Fenton/Fenton-like reactions under the GSH. (F) CLSM images of ROS generation after 4T1 cells were treated with different formulations. Scale bar $=$ 25 μm. (G) Quantitative analysis of the DCFH-DA fluorescent intensity in various conditions: (I) PBS group, (II) PBS + NIR, (III) GNRs@JQ1/ZIF-8, (IV) GNRs@FAC/ZIF-8, (V) GNRs + NIR, (VI) GNRs@JF/ZIF-8 and (VII) GNRs@JF/ZIF-8 +NIR, respectively. (H) Intracellular GSH depletion with different concentrations of GNRs@JF/ZIF-8 (0, 50 and 100 μg/mL).

viability of 4T1 cells was sequentially decreased because of the evidently boosted photothermal ferrotherapy. Subsequently, the cellular viability of the optimal formulation GNRs@JF/ZIF-8 at different concentrations (0, 20, 40, 60, 80, and 100 μg/mL) was detected (Fig. 3B). As expected, the cellular viability overall dropped with the increased concentrations, specifically, it was decreased to 19.6% under the 1064 nm laser irradiation at the concentration of 100 μg/mL, manifesting the brilliant efficiency of tumor therapy. Meanwhile, the calculated hemolysis ratio of GNRs@JF/ZIF-8 was less than 4% at the maximum concentration (100 μg/mL), demonstrating the hemocompatible property of GNRs@JF/ZIF-8 (Fig. 3C).

Furthermore, calcein-AM/PI fluorescence co-staining was applied to differentiate living (green) and dead (red) cells directly (Fig. 3D). The CLSM images exhibited dominating red color in GNRs@JF/ZIF-8 + NIR-treated group, while other laser-free groups showed limited cell death, representing that the laser-plus strategy magnified the tumor killing efficiency.

Besides, 4T1 cells were incubated with FITC-labeled GNRs@JF/ZIF-8 at different time points (1, 2, 6 and 12 h) to

detect the cellular uptake capacity (Supporting Information Fig. S10). The red and green fluorescence signals of Lysotracker Red and FITC-labeled GNRs@JF/ZIF-8 were detected, respectively, illustrating the internalization of GNRs@JF/ZIF-8 through endolysosome pathway. Consequently, the fluorescence signal of FITC-labeled GNRs@JF/ZIF-8 exhibited the highest intensity at 10 h incubation, while it decreased after 12 h incubation according to the CLSM images.

3.8. ROS-augmented FPT detection

Then, to verify the ROS/iron caused FPT pathway *via* Fenton/Fenton-like reactions, the total intracellular produced ROS in different formulations was evaluated by fluorescent DCFH-DA. As illustrated in Fig. 3F, FAC could be reduced by GSH and then reacted with H_2O_2 to produce ROS by Fenton/Fenton-like reactions. After culturing 4T1 cells with different groups, the PBS group (with and without NIR) exhibited negligible green fluorescence signal compared to the JQ1-free group of GNRs@JF/ZIF-8 and iron-free group of GNRs@JF/ZIF-8. As the PTT

control group, GNRs + NIR showed weaker fluorescence signal compared to GNRs@JF/ZIF-8-treated group. However, ROS production was significantly augmented by both JQ1 and FAC, which was further enhanced through the photothermal effect of the GNRs under the laser irradiation, illustrating that PTT effect could elevate the Fenton/Fenton-like reactions (Fig. 3F−G).

We then used the GSH Assay kit to measure the level of intracellular GSH depletion after incubated with different concentrations of GNRs@JF/ZIF-8 (Fig. 3H). GSH was consumed more than 63.0% after the addition of GNRs@JF/ZIF-8 (100 µg/mL), demonstrating that it could react with GSH in the tumor microenvironment (TME).

3.9.   BRD$_4$-downregulated FPT analysis by Western blot assay

To examine JQ1 caused FPT pathway illustrated in Fig. 4A, 4T1 cells were investigated by the Western blot analysis after treated with various formulations. As shown in Fig. 4B, there was no obvious change in PBS group (group I), while the expression levels of super-enhancer BRD$_4$ and ROS eliminator GPX4 were prominently down-regulated from group II to V as the concentration of GNRs/JQ1/ZIF-8 increased (20, 40, 60, and 80 µg/mL), thus inducing the elimination of ROS in tumor cells to further enhance LPO accumulation. Moreover, the GNRs/JQ1/ZIF-8 + NIR (80 µg/mL, group VI)-treated group sequentially

suppressed the expression of BRD$_4$ and GPX4, indicating that the heat could accelerate the release of JQ1 from the nano-matchbox (Fig. 4C).

3.10.   Cellular characteristic determination of FPT

In the present studies, FPT is featured with enhanced mitochondrial fragment and loosened mitochondrial membrane potential (MMP)[46−48], which could be detected by the indicator of JC-1 dye. When the MMP is high, JC-1 aggregates suggest red fluorescence signal, while JC-1 monomer produces green fluorescence signal when the potential is low. The drop of MMP is considered as a sign of FPT-induced mitochondrial damage in the light of the proportional changes of red and green fluorescence. In this study, after 4T1 cells were respectively incubated with: (I) PBS (control), (II) PBS + NIR, (III) GNRs@JQ1/ZIF-8, (IV) GNRs@FAC/ZIF-8, (V) GNRs + NIR, (VI) GNRs@JF/ZIF-8 and (VII) GNRs@JF/ZIF-8+NIR for 24 h, the CLSM images of PBS (with and without NIR) group exhibited the normal MMP, while CLSM images from group III to IV presented that the green and red fluorescence were gradually enhanced and decreased, respectively (Fig. 4D). Additionally, weak mitochondrial damage exhibited in group V due to the PTT effect. Meanwhile, group VII showed the most dramatic MMP drop compared with other groups, which was identified by the increased JC-1 monomer/aggregate ratio
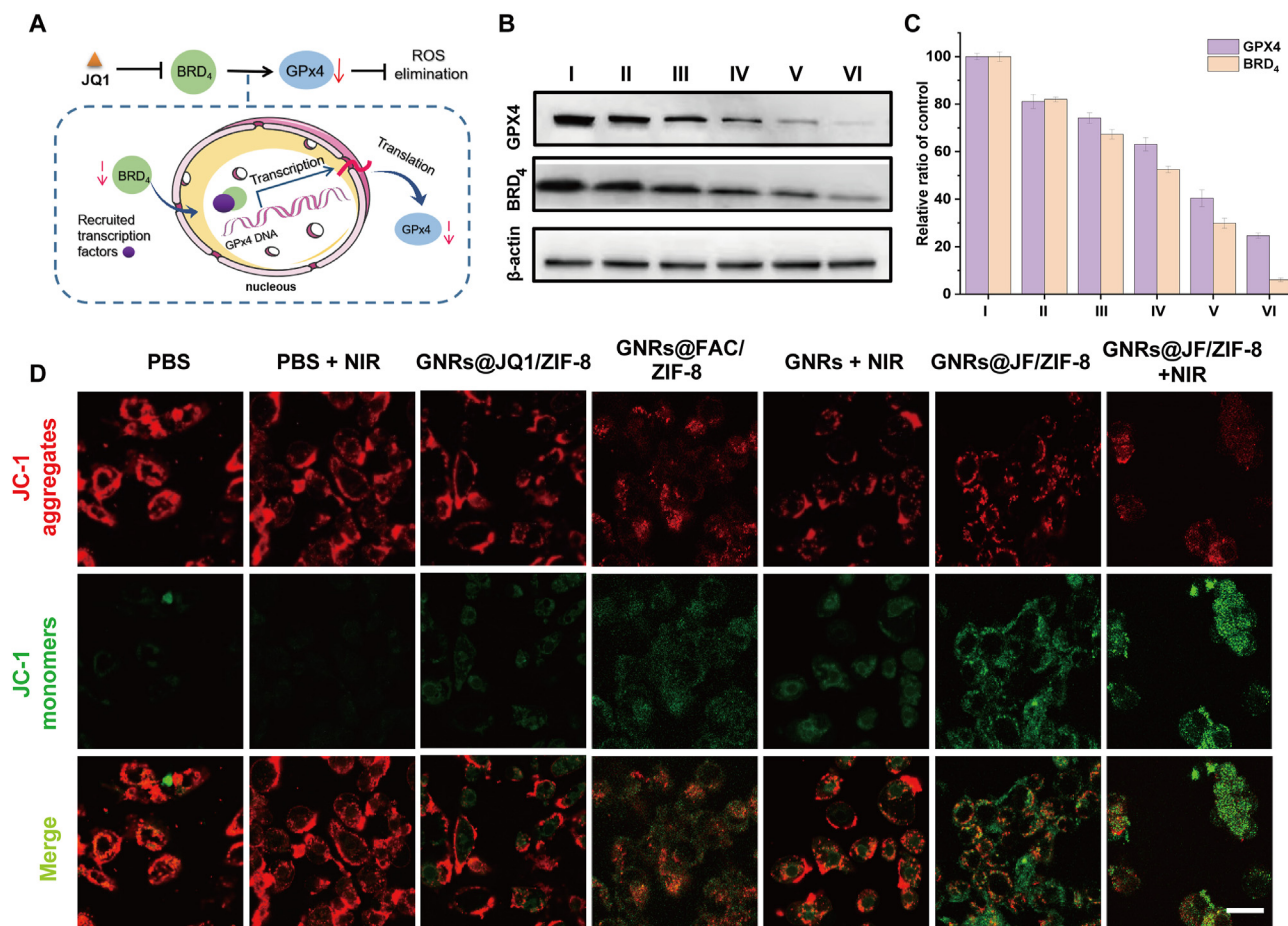

Figure 4   (A) Schematic illustration of the JQ1-induced ferroptosis. (B) Western blot assay for FPT-related protein levels. (C) Quantitative analyses of BRD$_4$ and GPX4 expression corresponding to (B) Groups (I)−(VI) in (C) referred to: (I) PBS, (II) 20 µg/mL GNRs@JQ1/ZIF-8, (III) 40 µg/mL GNRs@JQ1/ZIF-8, (IV) 60 µg/mL GNRs@JQ1/ZIF-8, (V) 80 µg/mL GNRs@JQ1/ZIF-8 and (VI) 80 µg/mL GNRs@JQ1/ZIF-8+NIR. (D) Mitochondrial membrane potential of 4T1 cells after treated with different groups. Scale bar = 25 µm.

(I:II:III:IV:V:VI:VII = 0.15:0.12:0.48:0.62:0.54:1.42:1.82), manifesting the highest degree of the photothermal ferrotherapy in the optimal treatment group (VII) (Supporting Information Fig. S11).

We then use Bio-TEM to intuitively investigate the FPT-induced damages of mitochondria before and after treatment. Simply, 4T1 cells were treated with PBS group and formulation of GNRs@JF/ZIF-8+NIR (1.0 W/cm², 5 min) for 12 h. As displayed in Fig. 5A, compared with the PBS group (group I, green arrows), the mitochondrial morphology analysis of 4T1 cells by TEM confirmed that the GNRs@JF/ZIF-8+NIR group (group II, blue arrows) induced more significant mitochondrial fragmentation and decreased mitochondrial size, which were the specific features for FPT.

Subsequently, the productions of intracellular LPO by 4T1 cells were quantified by a specific fluorescence probe named Liperfluo under the same culturing conditions. Consistent with the MMP assay, stronger fluorescence intensity was exhibited in the GNRs@JQ1/ZIF-8-treated group compared to PBS and PBS + NIR groups due to the LPO generation, while similar intensity was presented in GNRs@FAC/ZIF-8-treated group on account of the direct supplement of ROS and iron by FAC-induced Fenton/Fenton-like reactions. GNRs + NIR-treated group exhibited the weak fluorescence due to the ROS elevation by PTT effect. Comparatively, the GNRs@JF/ZIF-8-treated group was more powerful in provoking LPO accumulation than the other

groups, which owed to the combination of PTT and FPT effects (Fig. 5B).

3.11. In vitro/in vivo MSOT and CT imaging

The nano-matches like GNRs were applied as good CT and MSOT imaging agents for their simple surface chemistry, high X-ray attenuation and good biocompatibility. In our work, the GNRs@JF/ZIF-8 was also endowed with the MSOT/CT dual-mode imaging. For the in vitro MSOT imaging, the GNRs@JF/ZIF-8 exhibited dose-dependent signals with a linear relationship between concentrations and signal intensities (Supporting Information Fig. S12). Besides, in vitro CT contrast efficacy measurement of GNRs@JF/ZIF-8 with various concentrations (25, 50, 100, 200, 400 μg/mL) revealed a positive correlation between CT value and GNRs@JF/ZIF-8 concentrations (Supporting Information Fig. S13).

Subsequently, motivated by the excellent imaging efficiency in vitro, we then explored the feasibility of the GNRs@JF/ZIF-8 for MSOT and CT dual-mode imaging in vivo, in which 4T1-tumor-bearing mice were chosen as the animal model. Both MSOT and CT signals were recorded at various time points (1, 6, 12, and 24 h) after i.v. injection with PBS (control) and GNRs@JF/ZIF-8. From Fig. 6A−B images where the yellow dotted circles indicated the highlight of the signal accumulation in
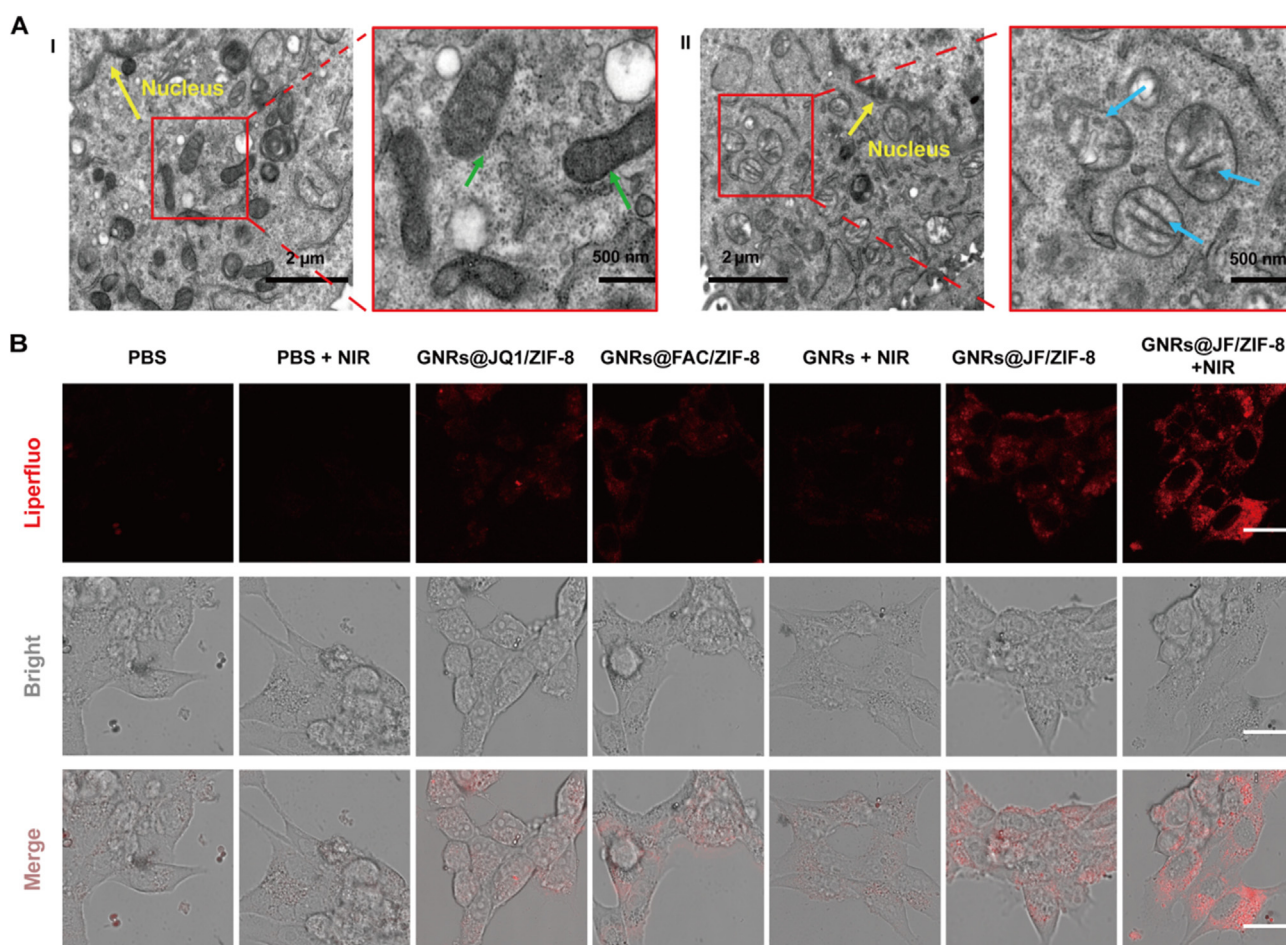

Figure 5 (A) Transmission electron microscope (TEM) images of mitochondria in 4T1 cells treated with (I) PBS and (II) GNRs@JF/ZIF-8+NIR. (B) Lipid peroxides in 4T1 cells under different treatments and detected by Liperfluo probes. Scale bar = 25 μm.
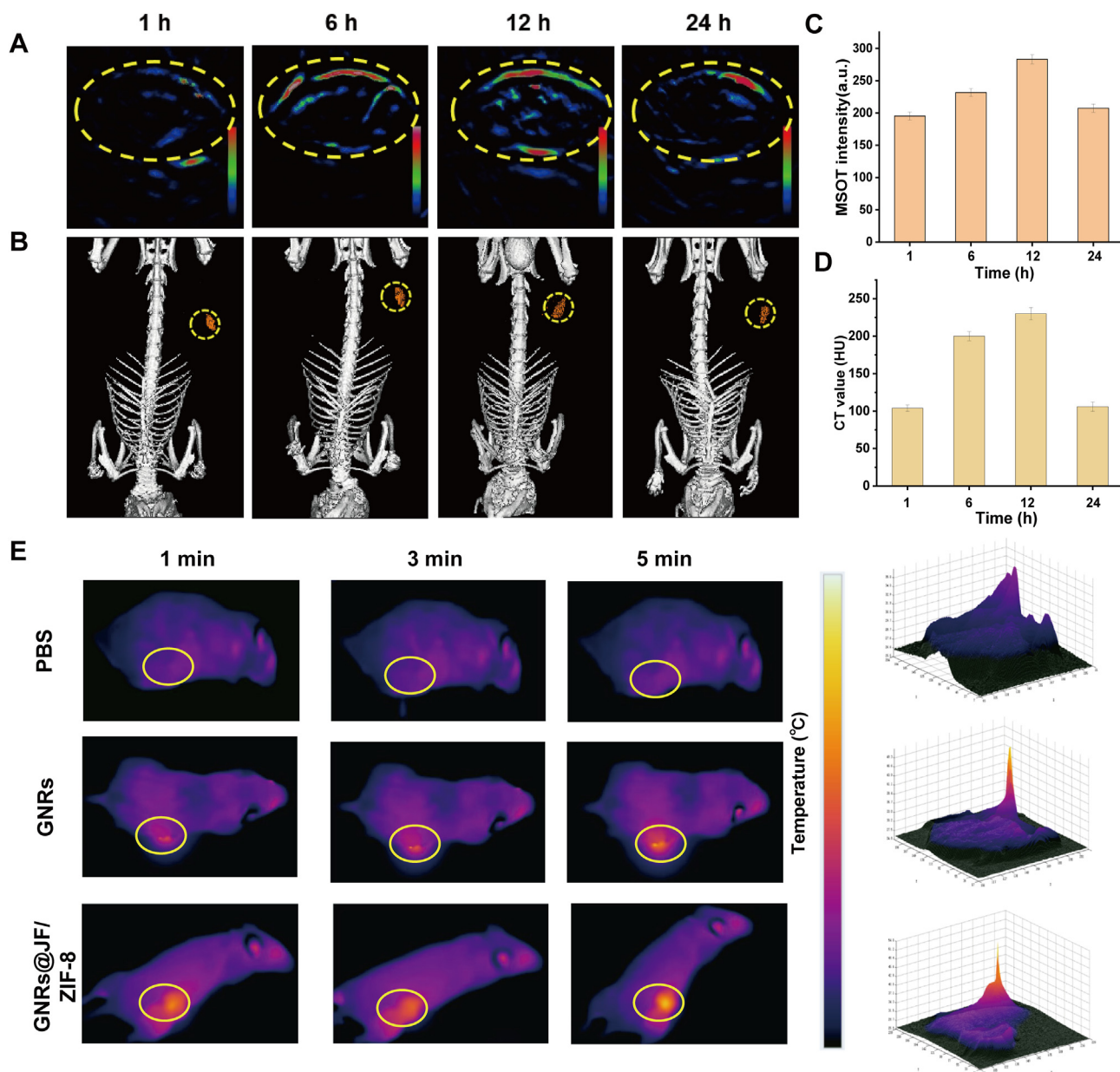
Figure 6 *In vivo* (A) MSOT and (B) CT images of tumor-bearing mice after i.v. injection of GNRs@JF/ZIF-8 at different times. (C) *In vivo* MSOT intensity and (D) CT value at different time. (E) Infrared thermographic images of tumor-bearing mice exposed to the 1064 nm laser after i.v. injection of GNRs and GNRs@JF/ZIF-8.

the tumor site and the corresponding MSOT and CT intensities (Fig. 6C–D), we could clearly observe the enhanced MSOT and CT signals accumulated in the tumor site and reached maximum at 12 h. However, weaker signals still could be detected after 24 h, indicating the long-time retention of the GNRs@JF/ZIF-8. Moreover, we compared the CT contrast capability of GNRs@JF/ZIF-8 with iopromide *in vivo*. After i.v. injection of the GNRs@JF/ZIF-8, the CT signal around the tumor site was greatly enhanced and exhibited blood circulation time (>12 h), while the commercial CT contrast agent iopromide would be cleared within a short time (<6 h). When the signal reached peak, both GNRs@JF/ZIF-8 and iopromide appeared clear visualization at

the tumor sites (Supporting Information Fig. S14), which portended that the GNRs@JF/ZIF-8 could be used as hopeful CT contrast agents.

3.12. *In vivo tumor therapy studies of GNRs@JF/ZIF-8*

On the basis of the photothermal efficiency of the GNRs@JF/ZIF-8 *in vitro*, the hyperthermia effect in 4T1-tumor-bearing mice were further investigated to monitor the temperature changes utilizing a thermal camera after intravenous injection and 1064 nm laser (1.0 W/cm^2, 5 min) irradiation. Specifically, the local temperature of GNRs and GNRs@JF/ZIF-8-treated mice were rapidly
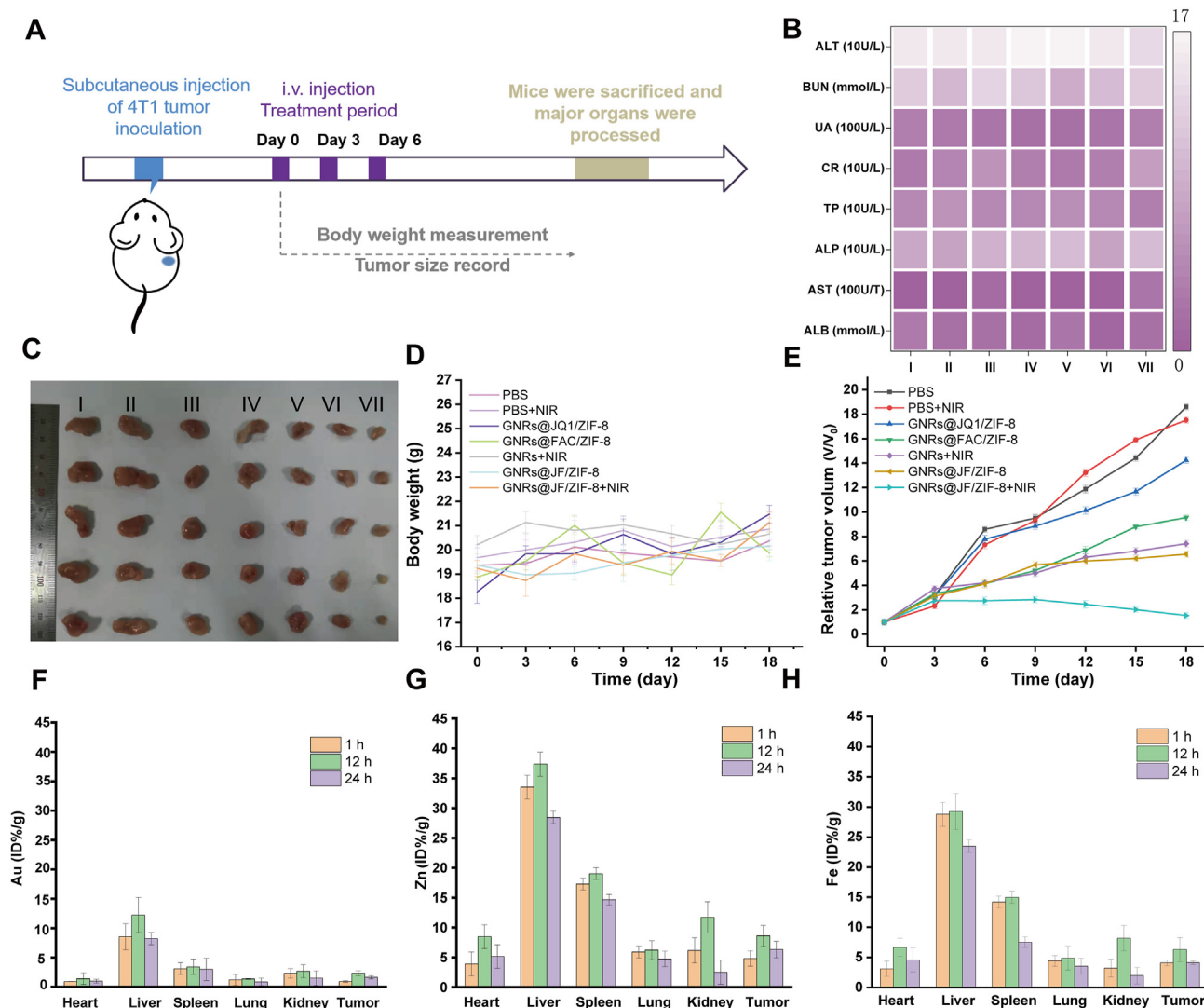
Figure 7 (A) Schematic illustration of tumor therapy studies *in vivo*. (B) The blood chemistry analysis of mice after treated with: (I) PBS, (II) PBS + NIR, (III) GNRs@JQ1/ZIF-8, (IV) GNRs@FAC/ZIF-8, (V) GNRs + NIR, (VI) GNRs@JF/ZIF-8 and (VII) GNRs@JF/ZIF-8+NIR. (C) Images of tumor tissues peeled from mice treated with various formulations. (D) Relative tumor volume curves of tumor-bearing mice in various treatment groups. (E) Body weight changes of mice with 4T1 tumors in different therapeutic groups. (F–H) The biodistribution of Au, Zn, Fe in tumors and main organs of mice after intravenous injection with GNRs@JF/ZIF-8 at different time.

increased up to 52.7 °C and 50.1 °C, which showed excellent PTT efficiency. However, the tumor surface of PBS-treated mice showed slightly elevated temperature (3−4 °C) (Fig. 6E).

Encouraged by the favorable biocompatibility and available therapeutic potential of GNRs@JF/ZIF-8 *in vitro*, the *in vivo* tumor-killing efficiency was determined accordingly. Briefly, after inoculated with 4T1 cells, the tumor-bearing mice with tumor volumes reached around 100 mm^3 were randomly separated into 6 groups and intravenously administered various formulations as follows: (I) PBS, (II) PBS + NIR, (III) GNRs@JQ1/ZIF-8, (IV) GNRs@FAC/ZIF-8, (V) GNRs + NIR, (VI) GNRs@JF/ZIF-8, and (VII) GNRs@JF/ZIF-8+NIR (Fig. 7A). During the period of tumor therapy, the relative tumor volume changes and the body weight of mice were persistently recorded every 2 days. As illustrated in Fig. 7C and D, there was barely any inhibitory action

on tumor growth in PBS groups (with or without NIR), whereas slight shrinkage of the tumor sizes was revealed in JQ1-free group (III, GNRs@FAC/ZIF-8) and iron-free group (IV, GNRs@JQ1/ ZIF-8), which demonstrated the insufficiency FPT therapy induced by single FAC or JQ1. Obvious shrinkage of tumors was exhibited in GNRs plus laser group, which verified the good photothermal therapeutic effect. However, the GNRs@JF/ZIF-8-treated group could also control the growth of tumor to a larger extent due to the accumulation of LPO caused by simultaneous FAC-induced ROS/iron increase and JQ1-downregulated ROS elimination. In addition, the optimal treatment of GNRs@JF/ZIF-8 + NIR could evidently reinforce the tumor growth compared with laser-free groups, which confirmed that the NIR-II could boost the FPT degree to accelerate the therapeutic effect (Supporting Information Fig. S15).
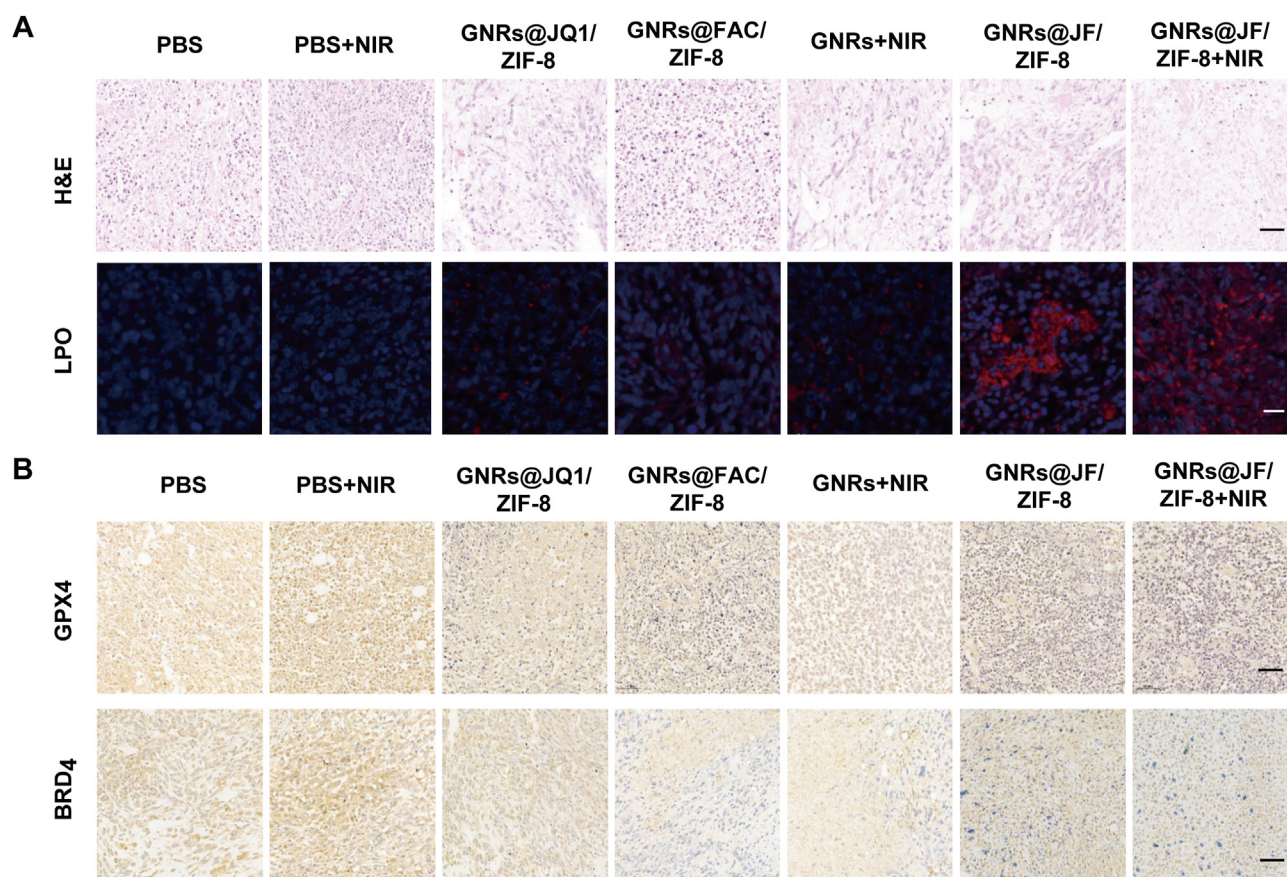
Figure 8 Microscopic images of (A) H&E staining, (B) immunofluorescent staining assays (LPO), and (C) immunohistochemically stained BRD4 and GPX4 expression of tumor tissues after different treatments. Scale bar = 25 μm.

3.13. The toxicology analysis of GNRs@JF/ZIF-8

We then examined the toxicology analysis of GNRs@JF/ZIF-8 through blood biochemical analysis, biodistribution, as well as H&E, immunofluorescent and immunohistochemical staining.

We initially determined various blood-index of different formulations-treated mice, including albumin (ALB), blood urea nitrogen (BUN), uric acid (UA), creatinine (CR), total protein (TP), alkaline phosphatase (ALP), aspartate transaminase (AST) and alanine aminotransferase (ALT). Apparently, there were no significant fluctuations in the hematological indicators of the treated groups compared with PBS group (control) (Fig. 7B), which suggested good hemocompatibility of GNRs@JF/ZIF-8 *in vivo*. Moreover, there was no significant change of body weight, which signified the low systemic side effects of GNRs@JF/ZIF-8 during the therapeutic process (Fig. 7E).

Furthermore, the biodistribution of GNRs@JF/ZIF-8 was comprehensively detected through intravenous administration. Tumors and major organs were eventually collected at 1, 12 and 24 h, in which Au, Zn and Fe contents could be measured by ICP−MS for a quantitative analysis of GNRs@JF/ZIF-8. It precisely showed that the reticuloendothelial systems like kidney,

liver and spleen were the main target organs (Fig. 7F−H). Moreover, the biodistribution data illustrated that the GNRs@JF/ZIF-8 could be accumulated in the tumor location with a high efficiency (2.32% of Au, 8.41% of Zn and 6.27% of Fe) at 12 h, which was probably due to the enhanced permeability and retention effect (EPR).

For histological hematoxylin & eosin (H&E) staining, no significant tissue damages were found in the main organs of GNRs@JF/ZIF-8+NIR-treated groups compared with the PBS group (Supporting Information Fig. S16). Nevertheless, the tumor tissues in GNRs@JF/ZIF-8 group showed obvious damages such as condensed nuclei and decreased intercellular space. In addition, NIR irradiation further facilitated the degree of these damages (Fig. 8A), which was consistent with the results of LPO staining (Fig. 8B).

Besides, it also exhibited the remarkably downregulated expression of FPT-related BRD$_4$ and GPX4 in GNRs@JF/ZIF-8+NIR-treated group compared with GNRs@FAC/ZIF-8 and GNRs@JQ1/ZIF-8 treatments, which further ensured the exclusive anti-tumor potency of GNRs@JF/ZIF-8+NIR in tumor microenvironment through LPO-induced ferrotherapy (Fig. 8C). The above results indicated that the GNRs@JF/ZIF-8 presented high biosafety and biocompatibility as well as efficient tumor-
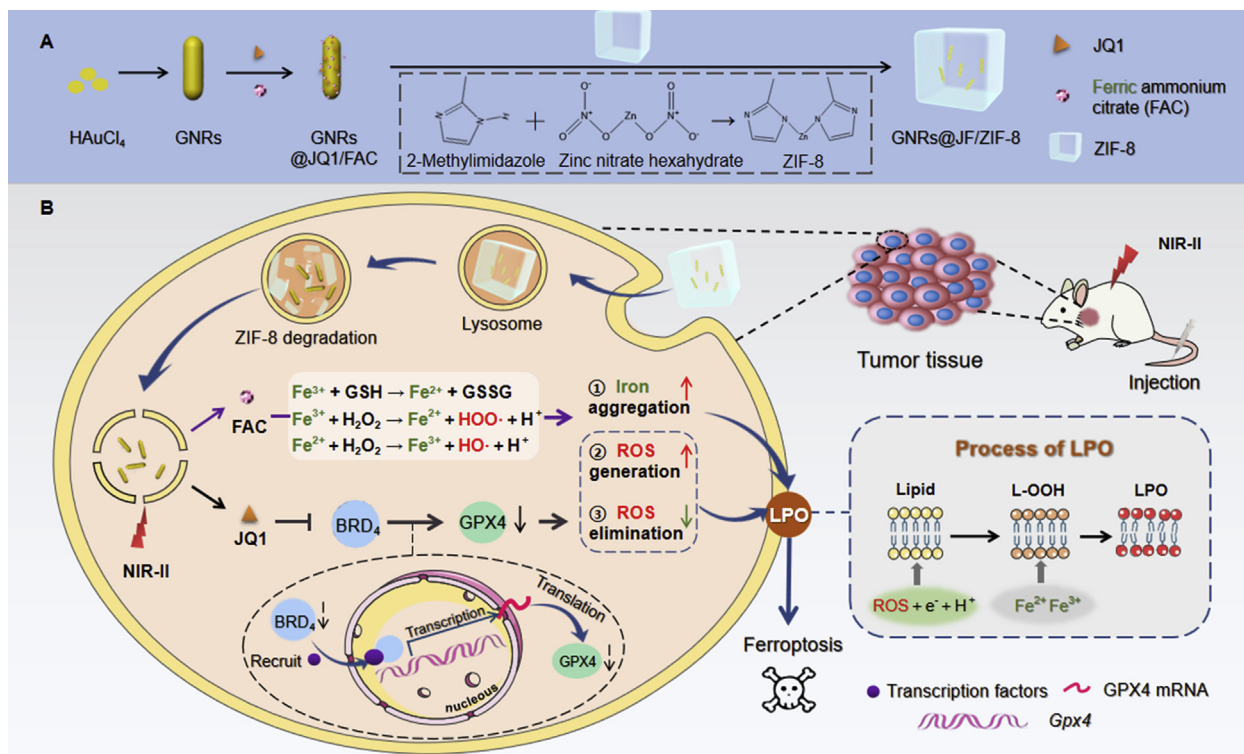
Scheme 1 Schematic illustrations of (A) the synthesis route of GNRs@JF/ZIF-8 and (B) amplified FPT therapy.

targeted capability, thus guaranteeing the application of amplified FPT in the tumor treatment.

4. Conclusions

In conclusion, we successfully design the matchbox-shaped nanoplatform GNRs@JF/ZIF-8 to exhibit extraordinary photothermal ferrotherapy effect, which based on JQ1/FAC-loaded and ZIF-8-coated GNRs. After internalizing into 4T1 tumor cells, the pH-sensitive ZIF-8 degrades in the lysosome acid condition while NIR-II-boosted hyperthermia results in PTT effect. Simultaneously, the released FAC (Fe^{3+}) is reduced to Fe^{2+} *via* GSH depletion and generates ROS through Fenton/Fenton-like reactions, which collectively augments the intracellular ROS and iron. On the other hand, the released JQ1 downregulates BRD_4 protein and suppresses ROS elimination based on the decreased GPX4 enzymatic activity. Eventually, this nanoplatform successfully synergizes NIR-II photothermal effect to elevate JQ1/FAC-amplified ferrotherapeutic effect. Besides, the potential of GNRs@JF/ZIF-8 as dual-imaging vehicle has been proven by monitoring strong MSOT and CT signals in tumor locations, which could be utilized to directly record the biodistribution of nanocomposites. As a result, the above advantages endow GNRs@JF/ZIF-8 with amplified photothermal ferrotherapy efficiency, which might motivate a promising exploitation of ferrotherapy pathway for tumor treatment.

Author contributions

Lujing Geng designed the research. Lujing Geng and Huaqing Jing carried out the experiments and performed data analysis. Tong Lu participated part of the experiments. Yue Zhou provided experimental drugs and quality control. Lujing Geng and Xiaoyang Liang wrote the manuscript. Lujing Geng and Yue Zhou revised the manuscript. All of the authors have read and approved the final manuscript.

Conflicts of interest

The authors have no conflicts of interest to declare.

Appendix A. Supporting information

Supporting data to this article can be found online at https://doi.org/10.1016/j.apsb.2022.05.011.

References

1. Galluzzi L, Bravo-San Pedro JM, Vitale I, Aaronson SA, Abrams JM, Adam D, et al. Essential *versus* accessory aspects of cell death: recommendations of the NCCD 2015. *Cell Death Differ* 2015;**22**:58−73.
2. Tang D, Kang R, Berghe TV, Vandenabeele P, Kroemer G. The molecular machinery of regulated cell death. *Cell Res* 2019;**29**:347−64.

3. Kerr JF, Wyllie AH, Currie AR. Apoptosis: a basic biological phenomenon with wide-ranging implications in tissue kinetics. *Br J Cancer* 1972;**26**:239−57.

4. Li D, Li Y. The interaction between ferroptosis and lipid metabolism in cancer. *Signal Transduct Targeted Ther* 2020;**5**:108.

5. He YJ, Liu XY, Xing L, Wan X, Chang X, Jiang HL. Fenton reaction-independent ferroptosis therapy *via* glutathione and iron redox couple sequentially triggered lipid peroxide generator. *Biomaterials* 2020;**241**:119911.

6. Shen Z, Song J, Yung BC, Zhou Z, Wu A, Chen X. Emerging strategies of cancer therapy based on ferroptosis. *Adv Mater* 2018;**30**: e1704007.

7. Stockwell BR, Friedmann Angeli JP, Bayir H, Bush AI, Conrad M, Dixon SJ, et al. Ferroptosis: a regulated cell death nexus linking metabolism, redox biology, and disease. *Cell* 2017;**171**:273−85.

8. Kagan VE, Mao G, Qu F, Angeli JP, Doll S, Croix CS, et al. Oxidized arachidonic and adrenic PEs navigate cells to ferroptosis. *Nat Chem Biol* 2017;**13**:81−90.

9. Doll S, Proneth B, Tyurina YY, Panzilius E, Kobayashi S, Ingold I, et al. ACSL4 dictates ferroptosis sensitivity by shaping cellular lipid composition. *Nat Chem Biol* 2017;**13**:91−8.

10. D'Herde K, Krysko DV. Ferroptosis: oxidized PEs trigger death. *Nat Chem Biol* 2017;**13**:4−5.

11. Yang WS, Stockwell BR. Ferroptosis: death by lipid peroxidation. *Trends Cell Biol* 2016;**26**:165−76.

12. Bao W, Liu X, Lv Y, Lu GH, Li F, Zhang F, et al. Nanolongan with multiple on-demand conversions for ferroptosis-apoptosis combined anticancer therapy. *ACS Nano* 2019;**13**:260−73.

13. Wang S, Li F, Qiao R, Hu X, Liao H, Chen L, et al. Arginine-rich manganese silicate nanobubbles as a ferroptosis-inducing agent for tumor-targeted theranostics. *ACS Nano* 2018;**12**:12380−92.

14. Shen Z, Liu T, Li Y, Lau J, Yang Z, Fan W, et al. Fenton-reaction-acceleratable magnetic nanoparticles for ferroptosis therapy of orthotopic brain tumors. *ACS Nano* 2018;**12**:11355−65.

15. Liu T, Liu W, Zhang M, Yu W, Gao F, Li C, et al. Ferrous-supply-regeneration nanoengineering for cancer-cell-specific ferroptosis in combination with imaging-guided photodynamic therapy. *ACS Nano* 2018;**12**:12181−92.

16. Zheng DW, Lei Q, Zhu JY, Fan JX, Li CX, Li C, et al. Switching apoptosis to ferroptosis: metal-organic network for high-efficiency anticancer therapy. *Nano Lett* 2017;**17**:284−91.

17. Hanahan D, Weinberg RA. Hallmarks of cancer: the next generation. *Cell* 2011;**144**:646−74.

18. Shibue T, Weinberg RA. EMT, CSCs, and drug resistance: the mechanistic link and clinical implications. *Nat Rev Clin Oncol* 2017;**14**:611−29.

19. Dixon SJ, Stockwell BR. The Hallmarks of ferroptosis. *Annu Rev Cell Biol* 2019;**3**:35−54.

20. Hangauer MJ, Viswanathan VS, Ryan MJ, Bole D, Eaton JK, Matov A, et al. Drug-tolerant persister cancer cells are vulnerable to GPX4 inhibition. *Nature* 2017;**551**:247−50.

21. Viswanathan VS, Ryan MJ, Dhruv HD, Gill S, Eichhoff OM, Seashore-Ludlow B, et al. Dependency of a therapy-resistant state of cancer cells on a lipid peroxidase pathway. *Nature* 2017;**547**:453−7.

22. Mai TT, Hamaï A, Hienzsch A, Caneque T, Muller S, Wicinski J, Cabaud O, et al. Salinomycin kills cancer stem cells by sequestering iron in lysosomes. *Nat Chem* 2017;**9**:1025−33.

23. Chen JJ, Galluzzi L. Fighting resilient cancers with iron. *Trends Cell Biol* 2018;**28**:77−8.

24. Liu H, Schreiber SL, Stockwell BR. Targeting dependency on the GPX4 lipid peroxide repair pathway for cancer therapy. *Biochemistry* 2018;**57**:2059−60.

25. Rennekamp AJ. The ferrous awakens. *Cell* 2017;**171**:1225−7.

26. Ward RJ, Zucca FA, Duyn JH, Crichton RR, Zecca L. The role of iron in brain ageing and neurodegenerative disorders. *Lancet Neurol* 2014;**13**:1045−60.

27. Tang Z, Liu Y, He M, Bu W. Chemodynamic therapy: tumour microenvironment-mediated Fenton and Fenton-like reactions. *Angew Chem Int Ed Engl* 2019;**58**:946−56.

28. Yao X, Yang P, Jin Z, Jiang Q, Guo R, Xie R, et al. Multifunctional nanoplatform for photoacoustic imaging-guided combined therapy enhanced by CO induced ferroptosis. *Biomaterials* 2019;**197**:268−83.

29. Yin H, Xu L, Porter NA. Free radical lipid peroxidation: mechanisms and analysis. *Chem Rev* 2011;**111**:5944−72.

30. Conrad M, Kagan VE, Bayir H, Pagnussat GC, Head B, Traber MG, et al. Regulation of lipid peroxidation and ferroptosis in diverse species. *Genes Dev* 2018;**32**:602−19.

31. Chen Q, Espey MG, Sun AY, Lee JH, Krishna MC, Shacter E, et al. Ascorbate in pharmacologic concentrations selectively generates ascorbate radical and hydrogen peroxide in extracellular fluid *in vivo*. *Proc Natl Acad Sci U S A* 2007;**104**:8749−54.

32. Zhang X, Zhang G, Zhang B, Su Z. Synthesis of hollow Ag-Au bimetallic nanoparticles in polyelectrolyte multilayers. *Langmuir* 2013;**29**:6722−7.

33. Sun M, Qian H, Liu J, Li Y, Pang S, Xu M, et al. A flexible conductive film prepared by the oriented stacking of Ag and Au/Ag alloy nanoplates and its chemically roughened surface for explosive SERS detection and cell adhesion. *RSC Adv* 2017;**7**:7073−8.

34. Daud NK, Ahmad MA, Hameed BH. Decolorization of acid red 1 dye solution by Fenton-like process using Fe−montmorillonite K10 catalyst. *Chem Eng J* 2010;**165**:111−6.

35. Gobouri AA. Ultrasound enhanced photocatalytic properties of α-Fe$_2$O$_3$ nanoparticles for degradation of dyes used by textile industry. *Res Chem Intermed* 2016;**42**:5099−113.

36. Debnath A, Deb K, Das NS, Chattopadhyay KK, Saha B. Simple chemical route synthesis of Fe$_2$O$_3$ nanoparticles and its application for adsorptive removal of Congo red from aqueous media: artificial neural network modeling. *J Dispersion Sci Technol* 2016;**37**:775−85.

37. Zhang L, Li J, Chu X, Zhao GC. Facile synthesis of Fe$_x$O$_y$/Ag nanocomposites for multifunctional and efficient catalytic applications. *J Cluster Sci* 2016;**27**:227−39.

38. Freyria FS, Bonelli B, Sethi R, Armandi M, Belluso E, Garrone E. Reactions of acid orange 7 with iron nanoparticles in aqueous solutions. *J Phys Chem C* 2011;**115**:24143−52.

39. Aijaz A, Karkamkar A, Choi YJ, Tsumori N, Rönnebro E, Autrey T, et al. Immobilizing highly catalytically active Pt nanoparticles inside the pores of metal−organic framework: a double solvents approach. *J Am Chem Soc* 2012;**134**:13926−9.

40. He L, Liu Y, Liu JZ, Xiong Y, Zheng J, Liu Y, et al. Core-shell noble-metal@metal-organic-framework nanoparticles with highly selective sensing property. *Angew. Chem Int EdEngl* 2013;**52**:3741−5.

41. Chen L, Luque R, Li Y. Encapsulation of metal nanostructures into metal-organic frameworks. *Dalton Trans* 2018;**47**:3663−8.

42. Zhao M, Yuan K, Wang Y, Li G, Guo J, Gu L, et al. Metal−organic frameworks as selectivity regulators for hydrogenation reactions. *Nature* 2016;**539**:76−80.

43. Suzuki H, Amano T, Toyooka T, Ibuki Y. Preparation of DNA-adsorbed TiO$_2$ particles with high performance for purification of chemical pollutants. *Environ Sci Technol* 2008;**42**:8076−82.

44. Vigderman L, Zubarev ER. Therapeutic platforms based on gold nanoparticles and their covalent conjugates with drug molecules. *Adv Drug Deliv Rev* 2013;**65**:663−76.

45. Wang XG, Dong ZY, Cheng H, Wan SS, Chen WH, Zou MZ, et al. A multifunctional metal-organic framework based tumor targeting drug delivery system for cancer therapy. *Nanoscale* 2015;**7**:16061−70.

46. Wang L, Jiang X, Ji Y, Bai R, Zhao Y, Wu X, et al. Surface chemistry of gold nanorods: origin of cell membrane damage and cytotoxicity. *Nanoscale* 2013;**5**:8384−91.

47. Jelinek A, Heyder L, Daude M, Plessner M, Krippner S, Grosse R, et al. Mitochondrial rescue prevents glutathione peroxidase-dependent ferroptosis. *Free Radic Biol Med* 2018;**117**:45−57.

48. An Y, Zhu J, Liu F, Deng J, Meng X, Liu G, et al. Boosting the ferroptotic antitumor efficacy *via* site-specific amplification of tailored lipid peroxidation. *ACS Appl Mater Interfaces* 2019;**11**:29655−66.